Fracture Mechanics of Ceramics

Active Materials, Nanoscale Materials, Composites, Glass and Fundamentals

Volume 1	Concepts, Flaws, and Fractography
Volume 2	Microstructure, Materials, and Applications
Volume 3	Flaws and Testing
Volume 4	Crack Growth and Microstructure
Volume 5	Surface Flaws, Statistics, and Microcracking
Volume 6	Measurements, Transformations, and High-Temperature Fracture
Volume 7	Composites, Impact, Statistics, and High-Temperature Phenomena
Volume 8	Microstructure, Methods, Design, and Fatigue
Volume 9	Composites, R-Curve Behavior, and Fatigue
Volume 10	Fracture Fundamentals, High-Temperature Deformation, Damage, and Design
Volume 11	R-Curve Behavior, Toughness Determination, and Thermal Shock
Volume 12	Fatigue, Composites, and High-Temperature Behavior
Volume 13	Crack–Microstructure Interaction, R-Curve Behavior, Environmental Effects in Fracture, and Standardization
Volume 14	Active Materials, Nanoscale Materials, Composites, Glass and Fundamentals

Fracture Mechanics of Ceramics

Active Materials, Nanoscale Materials, Composites, Glass and Fundamentals

Edited by

R. C. Bradt
University of Alabama
Tuscaloosa, Alabama

D. Munz
University of Karlsruhe
Karlsruhe, Germany

M. Sakai
Toyohashi University of Technology
Toyohashi, Japan

and

K. W. White
University of Houston
Houston, Texas

Springer

Proceedings of the 8th International Symposium on Fracture Mechanics of Ceramics, held February 25–28, 2003, at the University of Houston, Houston, Texas

ISSN: 0197-2766
ISBN-10: 0-387-24134-5 Printed on acid-free paper.
ISBN-13: 978-0387-24134-0

Printed in the United States of America.

9 8 7 6 5 4 3 2 1 (SPI/EB)

springeronline.com

CONTENTS

3. Fracture of Nano-Scale Materials

4. Composites

5. Fracture Fundamentals

6. Fracture of Coatings

7. Ferroelectric Materials

8. Reliability Prediction, Standardization and Design

PREFACE

The 8th International Symposium on fracture mechanics of ceramics was held on the campus of the University of Houston, Houston, TX, USA, on February 25-28, 2003. This marks three decades of progress in the science and technology development in ceramics since the first meeting of this group, held at the Pennsylvania State University in 1973, which was published in Volumes 1 and 2 of this series. The meetings continued over approximately four year intervals, held subsequently in Virginia Polytechnic Institute and State University, Japan Fine Ceramics Center, Nagoya, Japan, and Kernforschungszentrum, Karlsruhe, Germany.

With the natural maturing of the fields of structural ceramics, the present symposium has focused on nano-scale materials, composites, thin films and coatings as well as glass. The symposium also addressed new issues on fundamentals of fracture mechanics and contact mechanics, and a session on reliability and standardization.

The International Organizing Committee gratefully acknowledges the support from the Cullen College of Engineering, and the dedicated help from the local organizing committee. This includes Prof. L. Wheeler, Prashant Haldipur, Jennifer Husmo, Sandra Luna, Charlotte Palm and Jonathan Claydon. Additionally, I wish to thank the materials students who participated in the effort: Duo Liu, Mike Chelf, Marcos Flores, Rafael Longo and Yi Fang.

Special thanks are extended to NASA Astronaut Dr. Bonnie Dunbar for her wonderful banquet presentation.

Tuscaloosa, AL USA	R.C. Bradt
Karlsruhe, Germany	D. Munz
Toyohashi, Japan	M. Sakai
Houston, TX USA	K.W. White

ATOMIC FORCE MICROSCOPY AT ULTRASONIC FREQUENCIES

W. Arnold, A. Caron, S. Hirsekorn,
M. Kopycinska-Müller, U. Rabe, and M. Reinstädtler*

I. INTRODUCTION

Atomic Force Microscopy (AFM) is a near-field technique to generate high-resolution images of surfaces. A micro-fabricated elastic beam with an integrated sharp sensor tip at its end is scanned over the sample surface. With various dynamic modes, leading to Force Modulation Microscopy [1], Ultrasonic Force Microscopy [2], Atomic Force Acoustic Microscopy (AFAM) [3–5], Microdeformation Microscopy [6], Scanning Local Acceleration Microscopy [7] or Pulsed Force Microscopy [8], images can be obtained in which the contrast depends on the elasticity of the sample surface. However, quantitative determination of Young's modulus of a sample surface with AFM is a challenge, especially when stiff materials such as hard metals or ceramics are encountered. In this presentation the basic idea of AFAM, i.e. the evaluation of the cantilever vibration spectra at ultrasonic frequencies is discussed. The AFAM technique can be used for imaging as well as to discern local elastic data quantitatively. Nanocrystalline magnetic materials [9], multidomain piezoelectric materials and silicon [10], diamond-like carbon layers [11], polymeric materials and clay crystals [12] have been examined previously. The spatial resolution of the AFAM technique is approximately 10 nm.

In an Atomic Force Acoustic Microscopy set-up [3-5] either the sample is insonified or the cantilever suspension is excited at ultrasonic frequencies. The vibration spectra of the cantilever depend on the local sample stiffness and hence

---

* Fraunhofer-Institute for Nondestructive Testing (IZFP), Bldg. 37, University, D-66123 Saarbrücken, Germany

on the local elasticity of the sample constituents. Acoustic images can be obtained by measuring the cantilever vibration amplitude at a frequency close to a contact resonance or by monitoring the resonance frequency [13,14]. With this technique it is possible to resolve the differences in the local tip-sample stiffness between phases and/or grains having different crystal lattice orientation. In the case of ferroelectric materials the presence of the domains influences the local elastic properties within each individual grain. Depending on the method of sample preparation, for example etching, one can make domain patterns visible on the sample surface using AFM [15]. In this case the contrast is caused by topography. A variety of AFM techniques have been applied to image or modify the domains in ferro- electric single crystals as well as in thin films [16,17]. The AFAM technique allows domain structure imaging in single crystals and in ceramics, even when domains do not appear in the topography image [18]. Coupling the AFAM technique with the so- called piezo-mode [16,18–21] can additionally provide information about domain polarization and the orientation of the grains within the crystal lattice [20].

2. AFAM EXPERIMENTAL TECHNIQUE

An AFM cantilever clamped on one side and free on the other can be described as a micro-beam with a characteristic set of free resonance frequencies. The most common modes excited are either flexural or torsional. Values of the free flexural or torsional oscillations can be measured with e.g. an instrument such as a Dimension 3000 Nanoscope (Digital Instruments, Santa Barbara, Ca USA) or a Solver P47H (NT-MDT, Zelenograd, Russia) which were employed for this study. When the cantilever approaches the sample surface and finally touches it, the forces interacting between the cantilever tip and the surface modify the boundary condition of the vibrating cantilever [4,5]. As a result, the resonance frequencies shift to higher values. These resonance frequencies are called contact resonance frequencies (Fig. 1 and Fig. 2). The values of free and contact resonance frequencies can be calculated as discussed previously [4,5]. From the difference of the contact resonance frequencies relative to the free resonances, one obtains the vertical or lateral contact stiffness [5, 22] which itself depend on both the elastic moduli of the sample and the tip, and their Poisson ratio, respectively [23,24]. As shown in Fig. 1, the tip contacts the sample surface over a certain contact area which is inferred indirectly by using a calibration material of known elasticity. Detailed information about tip-sample interactions and methods of evaluating local tip-sample contact stiffness can be found elsewhere [9,10,25]. Under certain circumstances, the local elastic modulus or the so-called indentation modulus M [24] can be derived from the contact stiffness [9,10,18]. At present the contribution of adhesion forces to the contact stiffness is made small in AFAM measurements by applying a sufficiently high static force on the cantilever so that the Hertzian contact forces are dominant [23]. When evaluating the vertical contact stiffness, the lateral forces to k^* are neglected. The indented volume is about $\pi r_h^2 \times 3r_h \approx 500\,\mathrm{nm}^3$ where r_h is the contact radius, here about 10 nm or less.

The contact resonance frequencies are excited by an ultrasonic transducer, which emits longitudinal waves or shear waves into the sample. Figure 2 displays the normalized contact resonance spectra of the first (Fig. 2a) and second (Fig. 2b) flexural mode measured on fused quartz, silicon, and sapphire. The spring constant

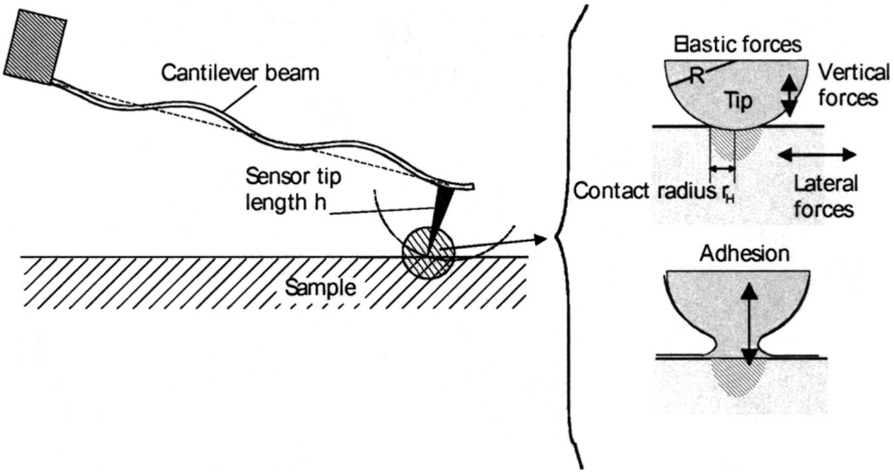

Figure 1. Principle of Atomic Force Acoustic Microscopy. Using the shift of the contact resonance frequencies relative to the free resonances, one can determine the local elastic constants of a material. The adhesion forces contribute to the measured vertical contact stiffness as well. Their influence can be neglected, provided the static forces are adjusted so that they are much larger than the adhesion forces.

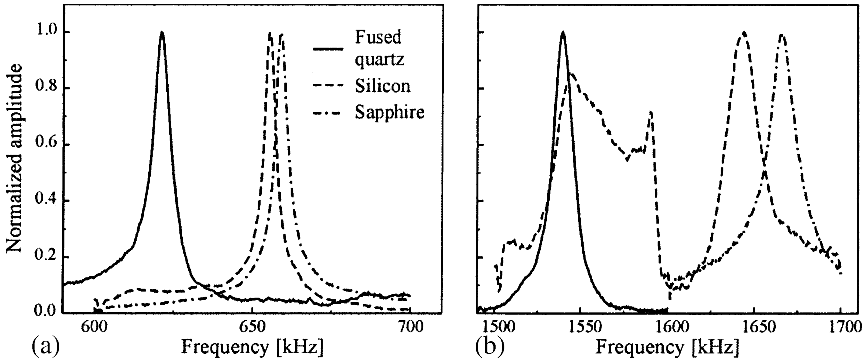

Figure 2. Normalized contact resonance spectra of the first (Fig. 2a) and second (Fig. 2b) flexural mode measured on samples with different elastic properties. The second mode on silicon shows a triple resonance.

of the cantilever was 44 N/m and the free resonance frequencies were 164 kHz and 1023 kHz for the first and second mode, respectively (not shown). The values of the indentation modulus of the reference samples varied from 77 (fused quartz), to 165 GPa (silicon), and to 423 GPa (sapphire). Very often double or triple resonance appear which are caused either by mode-coupling [26] or by multiple contacts between the tip and the surface.

In contact the resonance frequency varies during scanning and hence the amplitude and the phase of the cantilever vibration vary as well if the excitation frequency of the transducer is kept constant. This amplitude and phase contain information about the local tip-sample stiffness, and hence can be used as imaging quantities, see Fig. 3. It shows an AFAM-amplitude image of a lead calcium titanate film annealed at 650° C. The size of the images is $2 \times 2\,\mu\text{m}^2$. The cantilever material was coated with a conductive diamond-like layer. The overall spring constant was

44 N/m and the free resonance frequency of the first flexural mode of the cantilever was 188 kHz. The contrast seen in an amplitude image depends on the frequency of the applied ultrasound relative to the contact resonance frequency. At a frequency of 733 kHz the softer grains appear brighter than the stiffer grains (Fig. 3a). Imaging at a higher frequency, 791 kHz, the contrast of the image inverts (Fig. 3b) and the stiffer grains appear now brighter than the more compliant grains. This contract inversion has been known for a long time and has been noticed by several groups. Figure 4 shows an AFAM image of a nanocrystalline nickel sample based on monitoring the local contact resonance. From this measuring quantity, the local stiffness k^* is determined and then used as an imaging quantity. Values of the k^* ranged from 728 to 992 N/m. The tip used in this experiment was made from silicon, making it susceptible to tip wear [11]. The spring constant of the cantilever employed was 48 N/m and its free resonance frequencies were 166 and 1031 kHz for the first and second mode, respectively. The size of the image is 1.5 × 1.4 μm^2. The image clearly shows ensemble of grains in the nanocrystalline structure.

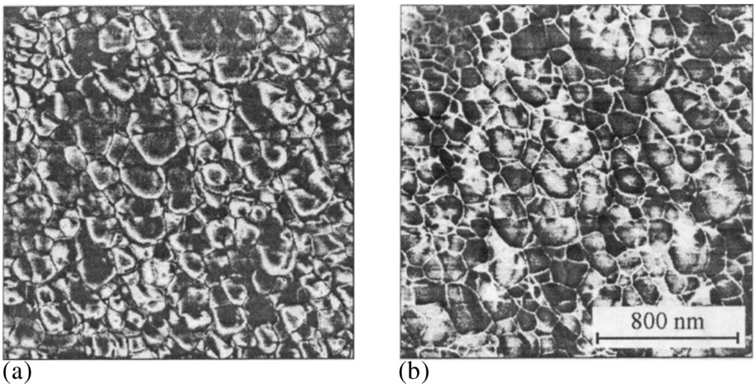

Figure 3. AFAM-amplitude images of a lead calcium titanate thin film annealed at 650° C. The contrast is caused by a shift of the resonance frequency when the contact stiffness changes locally. This in turn causes a change of the signal amplitude when the excitation frequency is kept constant.

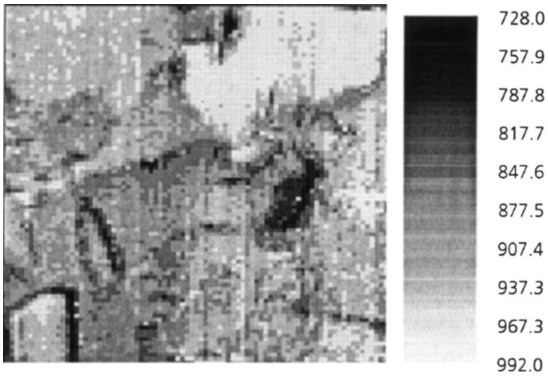

Figure 4. AFAM image of a nanocrystalline nickel sample. The contrast of the image is based on the contact stiffness comprising values between 728 N/m and 992 N/m. These values are determined from the contact resonances. The size of the image is 1.5 × 1.4 μm^2.

In the so-called piezo-mode of atomic force microscopy an ac voltage is applied to a conductive AFM cantilever while scanning the surface of a piezoelectric material. The tip of the cantilever senses the local deformation of the surface caused by the electric field between the tip and a counter electrode (Fig. 5b, see also Fig. 10). Usually the ac frequency is far below the free resonance frequency of the AFM cantilever [16,17,19,20]. In $BaTiO_3$, an image series based on vertical and torsional cantilever vibration signals of the same surface area allowed the reconstruction of the domain orientation using this mode [20].

The piezo-mode technique can also be performed at frequencies in the range of the first free resonance of the cantilever [27]. In the images shown here, the ac frequency was set equal to a contact resonance frequency [28] which entails resonance amplification increasing the contrast and signal-to-noise ratio in an image. Figures 6a and 6b show images in the AFAM and ultrasonic piezo-mode for comparison. In contrast to AFAM amplitude images, piezo-mode images do not show contrast inversion when the excitation frequency is varied. Furthermore it can be seen that in the piezo-mode image (Fig. 5b) that there are areas with no piezo-activity (area with question mark). Comparing Fig. 5a with Fig. 5b, one can notice that areas of higher tip-sample contact stiffness correspond to areas where there is vertical piezo-activity. This can only happen if the polarization of the domains is dominantly vertical. The dark area in the AFAM image corresponding to low tip-sample contact stiffness can either be caused by an in-plane orientation of the domains or because the film is not piezoelectric at such locations and hence not ferroelectric. Further investigations will follow.

As mentioned above rectangular AFM cantilever beams can also be forced to torsional vibrations. In this case the experimental set-up is such that an ultrasonic transducer emits shear waves into the sample causing in-plane surface vibrations. The shear wave transducer is oriented so that the surface vibrations are polarized perpendicular to the long axis of the cantilever. If low excitation amplitudes (0.1 nm) are applied and if the excitation frequency is set close to a contact resonance frequency, the amplitude and the phase of the cantilever vibration contain now information about the local lateral tip-sample stiffness. Used as imaging quantity, they yield images of shear stiffness. By increasing the lateral excitation amplitude much above

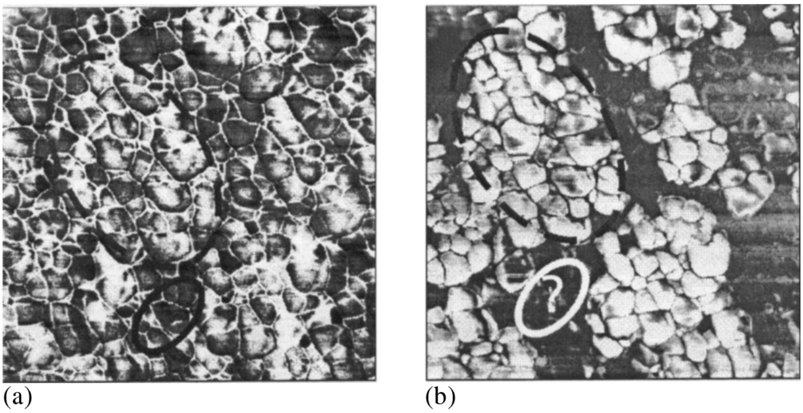

Figure 5. AFAM (a) and ultrasonic piezo-mode (b) images of the lead calcium titanate sample annealed at 650° C. The image in (a) is identical to the one in Fig. 3a.

0.1 nm, there is a change in the shape of the resonance curves. As shown recently [29] stick-slip between tip and sample occurs. This can be identified by taking local lateral spectra at one point of the sample: The maximum of the resonance curve increases linearly with the amplitude of the lateral displacement only at low excitation. At a certain threshold amplitude, the amplitude of the torsional vibrations does not increase any more and the resonance curve flattens out indicating the onset of sliding friction. Additionally, higher harmonics of the excitation signal appear which can be used for imaging. Such an image is shown in Fig. 6. A silicon sample was imaged first in the topography mode (Fig. 6a). At the excitation frequency of $f \approx 238\,\mathrm{kHz}$, an image was taken in the regime of stick-slip of the cantilever motion (Fig. 6b). Clearly an image could also be taken at 3f, here 714 kHz (Fig. 6c). It displays information related to the local friction coefficient. This new imaging mode is also at present the object of ongoing research.

3. APPLICATION OF AFM AND AFAM TO CRACK IMAGING

AFM and AFAM can be used to image cracks in ceramics in a similar way as can be done using SEM, Optical Microscopy or Scanning Acoustic Microscopy [30,31]. If one fractures a surface of a brittle material with a Vickers indenter, it is well-known and standard practice to infer from the length of the radial cracks the fracture toughness of the material [32]. There is much experience needed to determine reliably the length of the cracks with any of the microscopies. In this study the crack opening displacement U(x) was measured with an AFM. Measured close to the crack tip away from bridges in the wake of the crack, this would allow one to obtain information on K_{tip} using on the equation [33]

$$U(x) = \sqrt{8x/\pi}K_{\mathrm{tip}}/E' \tag{1}$$

Figs. 7a and 7b show AFM images of Si_3N_4 ceramics where fracture was caused in bending specimens of the size $3 \times 4 \times 25\,\mathrm{mm}^3$ by a 10 kg load using a Vickers indenter. The size of the images is $30 \times 30\,\mu\mathrm{m}^2$. One can clearly see the cracks, however, it was difficult to exactly determine the origin of the cracks. Using the routine "section analysis" of the DI 300 AFM instrument, U(x) was measured as a function of x. When evaluating the data, a possible offset for the exact position of

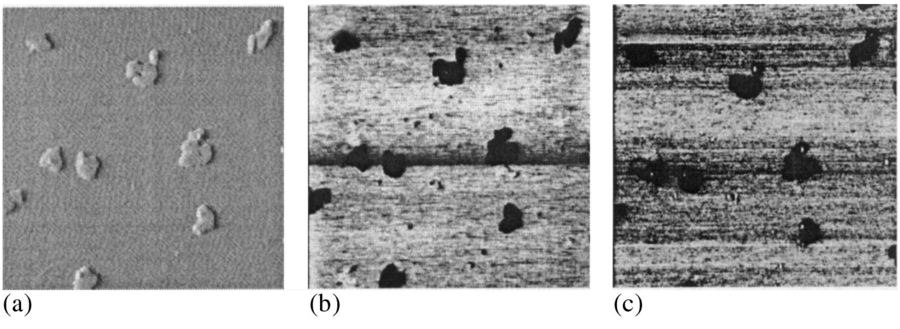
(a) (b) (c)

Figure 6. a) Topography of a Si-sample, b) Torsional amplitude $f = f_{\mathrm{excitation}}$, c) Torsional amplitude $f = 3 \times f_{\mathrm{excitation}}$.

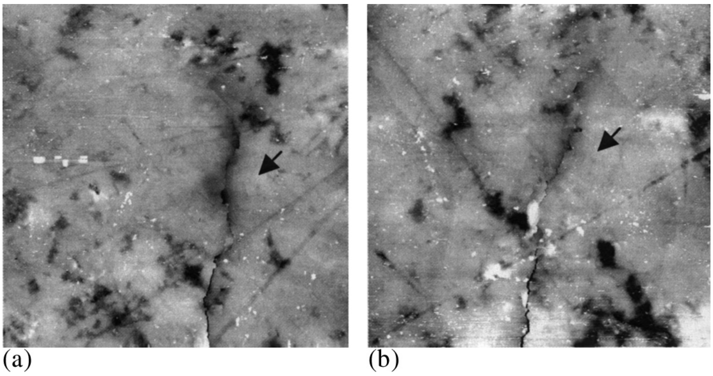

Figure 7. AFM topography images of two Si_3N_4 samples showing radial cracks caused by a Vickers indenter. The COD along the length of the radial cracks (arrows) was measured using standard routines of the DI instrument. A possible offset for the exact location of the tip was allowed in the analysis. The size of the image is 30H30 μm^2 and the topography scale was 120 nm (a) and 130 nm (b).

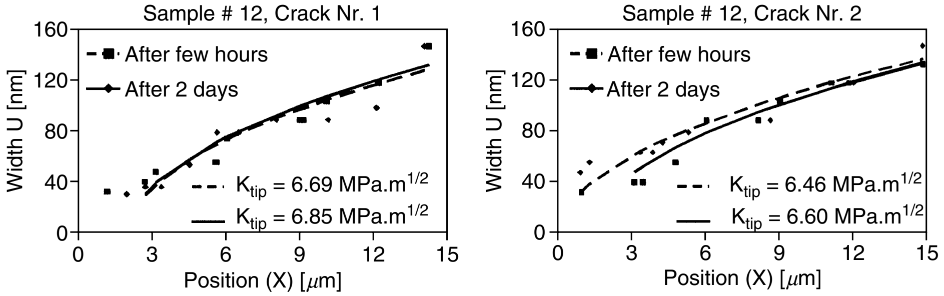

Figure 8. Crack opening displacement (COD) measured with an AFM in the topography mode. The figures display the width of the COD measured a few hours after the indent was made. The measurement was repeated after two days leading to a slight increase in the stress intensity factor. The data shown in Fig. 8a were obtained on the sample shown in Fig. 7a, and Fig. 8b corresponds to Fig. 7b.

the crack tip was taken into account. The reduced modulus E' for Si_3N_4 is 290 GPa. The value for K_{tip} was around 6.7 $MPam^{0.5}$ (Figs. 8) within the range of published data [32]. The high value indicates, however, that wake-effects played a role in the measurements, also the fact that the profile measured was not parabolic, see Figs. 8, as stipulated by Eq. (1)

We also studied in-situ crack propagation in an AFM by inducing cracks electrically, see Fig. 9. Poled PIC 151 PZT samples were loaded electrically with dc voltage of −900 V between the electrodes. Because the upper electrode was smaller than the ground electrode, an inhomogeneous electric field developed which was large enough to induce cracks due to the piezoelectric stresses.

Figure 10a shows a topography image of the environment of an individual crack in a crack field generated this way and Fig. 10b shows the corresponding AFAM image. Continued application of voltage led to additional cracking (Fig. 10c and 10d, arrow). Note that the AFAM images show also the domain structure opening the way to learn in-situ information on the role of the reorientation of domains in crack-shielding etc. which was much discussed during FCM8. Further studies are under way to clarify their role.

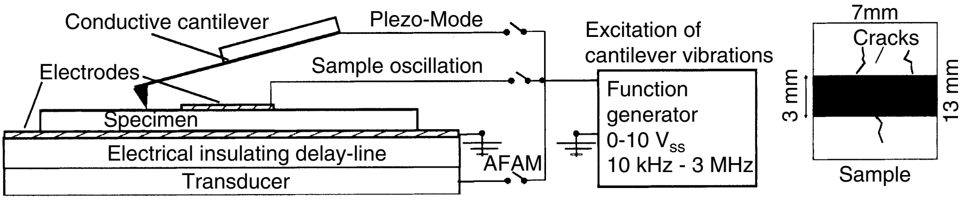

Figure 9. Configuration for the generation of in-situ cracks in an AFM allowing one to observe these cracks using the topography, the AFAM, and the ultrasonic piezo-mode. The insulating delay-line was necessary in order to protect the ultrasonic transducer from the applied dc voltages. The cracks emanate perpendicularly from the top electrode. The figure shows also the use of the electrodes for the ultrasonic piezo-mode.

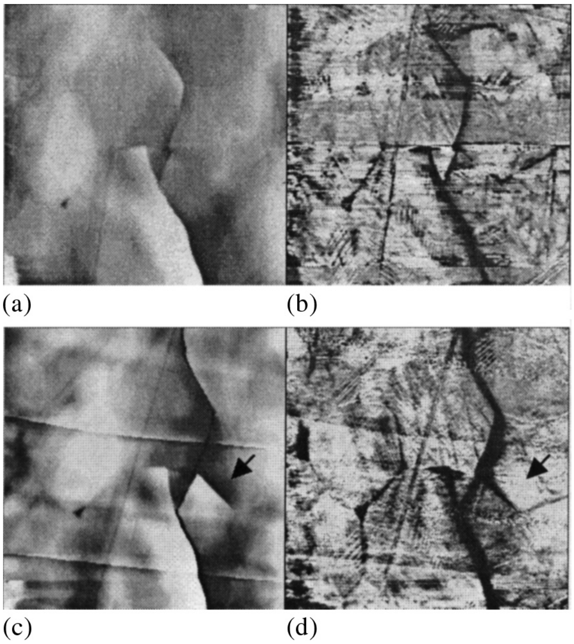

Figure 10. Observation of in-situ crack propagation after applying successive voltages up to −900 V to a PZT sample PIC 151; Fig. 10a: Topography image; Fig. 10b: AFAM image. The domain structure becomes visible. The images were taken with a cantilever having a spring constant of 47 N/m and at a static load of 1,8 μN. Continued voltage application leads to additional crack formation and reorientation of the domains (Fig. 10c and d, arrow). Image size of the individual images is 10H10 μm^2. The grey scale in the topography images comprises 70 nm.

Finally we studied crack propagation using the lateral stiffness as contrast in the images. Here the sensor tip vibrates in contact with the sample surface. An excitation frequency close to a torsional contact resonance frequency is selected. The torsional amplitude of the cantilever at this frequency is detected using the lateral channel of the AFM and a lock-in amplifier, and is then displayed as a color-coded image. A change in contact stiffness causes a shift of the contact resonance frequency and hence a change of cantilever vibration amplitude in the same manner as the vertical stiffness images, see above. Here also contrast inversion is observed. Cracks in a nanocrystalline ZrO_2 ceramic were generated by Vickers indents (Fig. 11). Fig. 11a

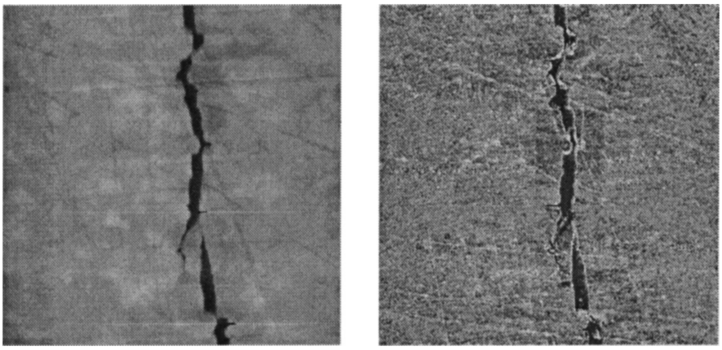

Figure 11. Topography (left) and lateral AFAM image (right) of a ZrO_2 ceramic.

shows topography, Fig. 11b the corresponding torsional resonance images of the identical surface areas. There are darker areas close to the crack flanks showing regions of altered elastic properties. This could be caused for example by the crack system below the surface and is examined further at present.

3. CONCLUSIONS

The AFAM and ultrasonic piezo-mode techniques described here lend itself for studying materials properties in ceramics on a nanoscale. Whereas the various imaging modes become more and more routine, the application of the AFM and ultrasonic AFM technique to study crack propagation are still in the early stage. However, the results presented here show that these techniques may provide much wanted information on the elastic, piezoelectric, and fracture mechanical behavior of ceramics during crack propagation.

4. ACKNOWLEDGEMENT

We gratefully acknowledge the financial support by the German Science Foundation. One of us (M.K-M) was supported by the SFB 277 at the University of the Saarland. Furthermore, it is a pleasure to thank D. Lupascu and J. Rödel for helpful discussions.

REFERENCES

1. P. Maivald, H.T. Butt, S.A. Gould, C.B. Prater, B. Drake, J.A. Gurley, V.B. Elings, and P.K. Hansma, Using Force Modulation to Image Surface Elasticities with the Atomic Force Microscope, *Nanotechnology* **2,** 103–106 (1991).
2. K. Yamanaka, H. Ogiso, and O. V. Kolosov, Ultrasonic force microscopy for nanometer resolution subsurface imaging, *Appl. Phys. Lett.* **64**, 178–180 (1994).
3. U. Rabe and W. Arnold, Acoustic Microscopy by Atomic Force Microscopy, in: *Proc. 21st Int. Symp. Acoustical Imaging*, edited by J. P. Jones, Plenum Press, New York, (1995) 585–592.

4. U. Rabe, K. Janser, and W. Arnold, Acoustic Microscopy with Resolution in the nm-Range, in: *Proc. 24th Int. Symp. Acoustical Imaging*, Eds. P. Tortoli, L. Masotti, Plenum Press, New York (1996) 669–676.
5. U. Rabe, K. Janser, and W. Arnold, Vibrations of Free and Surface-Coupled Atomic-Force Microscope Cantilevers: Theory and Experiment, *Rev. Sci. Instrum.* **67,** 3281–3293 (1996).
6. P. Vairac and B. Cretin, Scanning microdeformation microscopy in reflection mode, *Appl. Phys. Lett.* **68**, 461–463 (1996).
7. N.A. Burnham, G. Gremaud, A.J. Kulik, P.J. Gallo, and F. Oulevy, Scanning local-acceleration microscopy, *J. Vac. Sci. Tech.* **B14,** 794–799 (1996).
8. A. Rosa, E. Weilandt, S. Hild, and O. Marti, The simultaneous measurement of elastic, electrostatic and adhesive properties by scanning force microscopy: pulsed-force mode operation, *Meas. Sci. Technol.* **8,** 1333–1338 (1997).
9. E. Kester, U. Rabe, L. Presmanes, Ph. Tailhades, and W. Arnold, Measurement of Young's Modulus of Nanocrystalline Ferrites with Spinel Structures by Atomic Force Acoustic Microscopy *J. Phys. Chem. Solids* **61,** 1275–1284 (2000).
10. U. Rabe, S. Amelio, M. Kopycinska, S. Hirsekorn, M. Kempf, M. Göken, and W. Arnold, Imaging and Measurement of Local Mechanical Material Properties by Atomic Force Acoustic Microscopy, *Interf. and Surf. Analysis* **33,** 65–70 (2002).
11. S. Amelio, A. V. Goldade, U. Rabe, V. Scherer, B. Bhushan, and W. Arnold, Measurements of Elastic Properties of Ultra Thin Diamond-Like Carbon Coatings using Atomic Force Acoustic Microscopy, *Thin Solid Films* **392,** 75–84 (2001).
12. M. Prasad, M. Kopycinska, U. Rabe, and W. Arnold, Measurement of Young's Modulus of Clay Minerals Using Atomic Force Acoustic Microscopy, *Geophys. Res. Lett.* **29,** 13–16 (2002).
13. U. Rabe, S. Amelio, S. Hirsekorn, and W. Arnold, Imaging of Ferroelectric Domains by Atomic Force Acoustic Microscopy, in: *Proc. 25th Int. Symp. Acoustical Imaging*, edited by M. Halliwell and P.N.T. Wells, Kluwer Academic/Plenum Publishers, 253–260 (2000).
14. K. Yamanaka, Y. Maruyama, T. Tsuji, and K. Nakatomo, Resonance frequency and Q factor mapping by ultrasonic atomic force microscopy, *Appl. Phys. Lett.* **78,** 1939–1941 (2001).
15. A. L. Gruverman, J. Hatano, and H. Tokumoto, Scanning Force Microscopy Studies of Domain Structure in $BaTiO_3$ Single Crystals, *Jap. J. Appl. Phys.* **36,** 2207–2211 (1997).
16. P. Güthner and K. Dransfeld, Local poling of ferroelectric polymers by scanning force microscopy, *Appl. Phys. Lett.* **61**, 1137–1139 (1992).
17. A. Gruverman, O. Auciello, and H. Tokumoto, Scanning force microscopy: application to nanoscale studies of ferroelectric domains, *Integrated Ferroelectrics* **19,** 49–83 (1998).
18. U. Rabe, M. Kopycinska, S. Hirsekorn, J. Muñoz Saldaña, G.A. Schneider, and W. Arnold, High-resolution characterisation of piezoelectric ceramics by ultrasonic scanning force microscopy techniques, *J. Phys. D: Appl. Phys* **35,** 2621–2536 (2002).
19. K. Franke, J. Besold, W. Haessler, and C. Seegebarth, Modification and detection of domains on ferro-electric PZT films by scanning force microscopy, *Surf. Sci. Lett.* **302,** 283–288 (1994).
20. L. M. Eng, H.-J. Güntherodt, G. A. Schneider, U. Köpke, and J. Munoz Saldana, Nanoscale reconstruction of surface crystallography from three-dimensional polarization distribution in ferroelectric barium-titanate ceramics, *Appl. Phys. Lett.* **74,** 233–235 (1999).
21. S. Hong, J. Woo, H. Shin, J. U. Jeon, Y. E. Pak, E. L. Colla, N. Setter, E. Kim, K. No, Principle of ferroelectric domain imaging using atomic force microscope, *J. Appl. Phys.* **89,** 1377–1386 (2001).
22. V. Scherer, "*Ultraschall-Kraft-Mikroskopie mit lateraler Anregung*" Naturwisenschaftlich Technische Fakultät III. PhD-Thesis, University of the Saarland, (2002), unpublished.
23. K. L. Johnson, *Contact Mechanics* (Cambridge University Press, Cambridge, 1995).
24. G. M. Pharr, W. C. Oliver, F. Brotzen, On the generality of the relationship among contact stiffness, contact area, and elastic modulus during indentation, *J. Mat. Res.* **7,** 613–617 (1992).
25. K. Yamanaka, T. Tsuji, A. Noguchi, T. Koike, T. Mihara, Nanoscale elasticity measurement with in situ tip shape estimation in atomic force microscopy, *Rev. Sci. Instr.* **71,** 2403–2408 (2000).
26. M. Reinstaedtler, U. Rabe, V. Scherer, J.A. Turner, and W. Arnold, Imaging of flexural and torsional resonance modes of atomic force microscopy cantilevers using optical interferometry, *Surface Science*, (2003) in print
27. M. Labardi, V. Likodimos, and M. Allegrini, Force-microscopy contrast mechanisms in ferroelectric domain imaging, *Phys. Rev.* **B 61,** 14390–14398 (2000).

28. M. Kopycinska, U. Rabe, S. Hirsekorn, W. Arnold, Imaging of the Ferroelectric Domains Pattern in the Ultrasonic Piezo-Mode in: *Proc. 26th Acoustical Imaging, edited by R. Maev Kluwer Academic Publishers, New York, Acoustical Imaging*, **26,** 191–198 (2002).
29. M. Reinstädtler, U. Rabe, V. Scherer, U. Hartmann, A. Goldade, B. Bhushan, and W. Arnold, On the nanoscale measurement of friction using atomic-force microscope cantilever torsional resonances, *Appl. Phys. Lett.* **82,** 2604–2606 (2003).
30. W. Arnold, G. Weides, and S. Faßbender, Measurement of Elastic Properties Related to the R-Curve-Behavior of Ceramics, in: *Proc. of APCFS & ATEM '01 (Asian Pacific Conference on Fracture and Strength '01 and International Conference on Advanced Technology in Experimental Mechanics '01)*, The Japan Society of Mechanical Engineers, Tokyo, 2001, pp 517–522.
31. T.J. Marrow, G.A.D. Briggs, and S.G. Roberts, In-situ Acoustic Microscopy of Crack Bridging in Alumina, *J. Europ. Ceram. Soc.* **14,** 111–116 (1994).
32. B. Lawn, *Fracture of Brittle Solids*, in Cambridge Solid State Science Series (Cambridge University Press, 1995) pp. 249–306.
33. J. Rödel, J.F. Kelly, and B.R. Lawn, “In-situ Measurements of Bridging Crack Interfaces in the Scanning Electron Microscope”, *J. Am. Soc.* **73,** 3313–3318 (1990).

INDENTATION SIZE EFFECT ON THE HARDNESS OF ZIRCONIA POLYCRYSTALS

Takashi Akatsu, Shingo Numata, Michiyuki Yoshida,
Yutaka Shinoda, and Fumihiro Wakai*

1. INTRODUCTION

The hardness of materials is one of the most important mechanical properties from an engineering point of view. The hardening of metals is realized by the inhibition of dislocation glide, which can be managed through microstructural design. The Hall-Petch hardening $H \propto d^{-1/2}$, where H is the hardness and d is the grain size, is a well-known and useful concept of the design. Conversely, the inverse Hall-Petch relation is recently found out in a metal consisted of very fine grains.[1,2] Also, it is revealed that the H-value of metals does not depend on only d but indentation size, i.e. the hardness increases with a decrease in indentation size. The indentation size dependence is described through the building-up of geometrically necessary dislocations under a concentrated stress field.[3,4] In terms of ceramics, correlation between hardness and microstructure has not been cleared, although a lot of research has been done.[5,6] For example, even the grain size dependence of the hardness has not been generally described. The hardness of ceramic nanopolycrystals, which consists of very fine grains with a diameter less than 1μm, has not been examined in detail. Moreover, indentation size effect on the hardness has been scarcely reported. The experimental and theoretical difficulty to estimate the plasticity of a hard elastic-plastic material is one of the reasons for the obscurity in the hardness of ceramics. The development and improvement of the nanoindentation technique helps us to make an accurate evaluation of the plasticity of ceramics.

---

* Takashi Akatsu, Shingo Numata, Michiyuki Yoshida, Yutaka Shinoda, and Fumihiro Wakai, Materials and Structures Laboratory, Tokyo Institute of Technology, 4259 Nagatsuta, Midori, Yokohama 226–8503, Japan

In this study, the nanoindentation on monoclinic-, tetragonal- and cubic-zirconia polycrystals (referred as MZP, TZP and CZP, respectively) was carried out with a home-made nanoindenter. Relationship between indentation load P and penetration depth h of a diamond stylus was analyzed to derive the true hardness H_T as a function of the plastic depth h_p, which is a measure of plasticity.[7] The plastic deformation of each zirconia at room temperature was discussed in detail through the examination and the mutual comparison of indentation size dependence of H_T.

2. EXPERIMENTAL

2.1. Samples

The zirconia polycrystals with different crystallographic structure (monoclinic, tetragonal and cubic) were fabricated to be a fine structure. Three kinds of very fine zirconia powders, TZ-0Y, TZ-3Y and TZ-8Y (Tosoh Co.ltd. Japan), were sintered with HIP under 200MPa to make MZP, TZP and CZP, respectively.[8] The average grain size of as-sintered MZP, TZP and CZP, which was determined through SEM observation and the intercept method, was 60, 60 and 110nm, respectively. In addition, heat treatment of each zirconia was carried out to enlarge their grain size. Nanoindentation on the {100} plane of a single crystal of cubic zirconia (YSZ(100), Shinkosha Co.ltd., Japan) was also carried out in comparison. The mirror-finished surface of all samples was carefully prepared by polishing with colloidal silica powders with a diameter less than 60 nm.

2.2. Nanoindentation

Precise h measurement is very important for the accurate evaluation of hardness through the nanoindentation technique. External deformation due to the compliant structure of a conventional nanoindenter must be eliminated from h measured, because h is usually given as the drive of a diamond stylus towards the surface of a sample.[9] Some calibrations to compensate the extrinsic deformation are conventionally carried out, but they are, in many cases, poor at reproducibility. That is one of the reasons for the inaccurate hardness evaluation with the nanoindentation. In this study, the accurate value of h was directly measured by using a home-made nanoindenter with a unique system as shown in Fig.1. The difference between the drive and deflection of the beam fixed with the stylus (see Fig.1) definitely gives the accurate h without doing any calibrations. The P-value was determined as a function of the deflection and flexibility of the beam. In addition, vertical indentation within an error of ±0.1° was confirmed using a laser reflection displacement transducer (see Fig.1) and stages for the tilt and horizontal rotation of a sample. The system shown in Fig.1 was made of super invar alloy with a thermal expansion of $0.7 \times 10^{-6}/^{\circ}\mathrm{K}$ at room temperature to decrease the error due to the temperature change during indentation. Nanoindentation at room temperature in air was actually carried out by using the nanoindenter with the Berkovich-type diamond stylus at a penetration rate of 50nm/sec.

2.3. Analysis of *P-h* Curves

It is relatively hard to find ideal quadratic relation between P and h in the very shallow indentation region. That is attributed to the blunt tip of a diamond stylus,

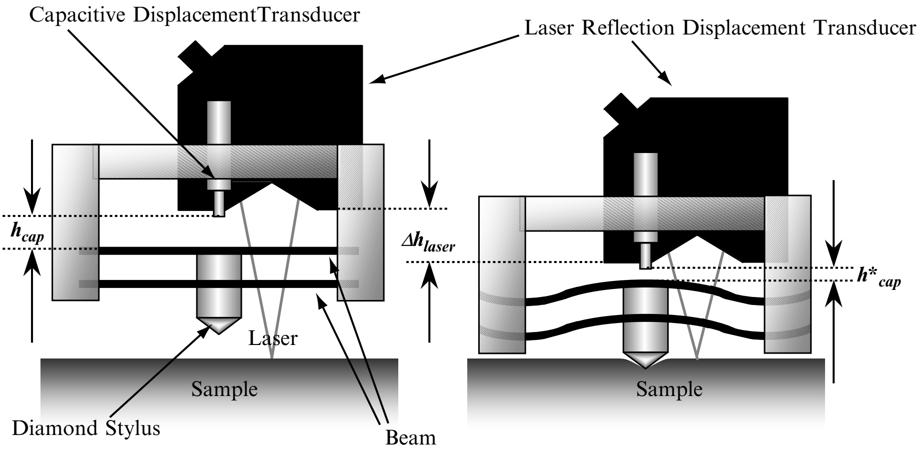

Figure 1. A unique system of a home-made nanoindenter to measure accurate P and h. The difference between the drive Δh_{laser} and deflection $\Delta h_{cap}(=h_{cap}\text{-}h^*_{cap})$ of the beam gives an accurate h. The P-value is given as a function of Δh_{cap} and the flexibility of the beam.

which causes the overestimation of hardness in that region. We made a two-step modification of P-h curves to avoid the overestimation at small h as follows: At first, loading and unloading P-h curves were transferred by the distance Δh between the real and ideal origins, which was determined by the extrapolation of linear relation between $P^{1/2}$ and h at relatively large h into $h = 0$, in the positive direction of h (see Fig. 2). Secondly, P-h data from $h = 0$ to $h > 2\Delta h$ for loading and from h_r to $h_r + 2\Delta h$ for unloading were neglected, respectively, in the following analysis (see Fig. 2). According to the Oliver and Pharr method,[10] the Meyer hardness H_M was derived from the modified P-h curves as follows,

$$H_M = \frac{P_{\max}}{g{h_c}^2} \tag{1}$$

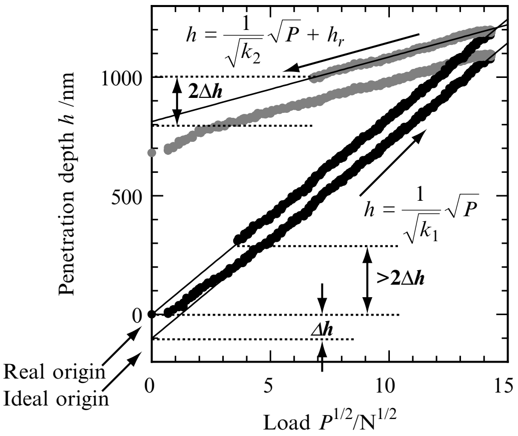

Figure 2. Modification of P-h curves to avoid the overestimation of hardness in the shallow indentation region due to the blunt tip of a diamond stylus.

$$h_c = h_{\max} - \varepsilon \frac{P_{\max}}{S} \tag{2}$$

where $P_{\max}$ the maximum indentation load, $h_{\max}$ the maximum penetration depth of the stylus, g the geometrical factor to be 24.5 for the Berkovich-type stylus, ε the constant to be 0.72 for conical stylus, and S the unloading slope at $P_{\max}$. An analysis to derive H_T and h_p^9 was also carried out for the modified $p^{1/2}$-h relationship as follows,

$$H_T = \frac{k_1/\left(g/\gamma_p{}^2\right)}{\left(1 - \sqrt{k_1/k_2}\right)^2} \tag{3}$$

$$h_p = \sqrt{\frac{P\gamma_p{}^2}{gH_T}} \tag{4}$$

where k_1 and k_2 are the linear slopes of $P^{1/2}$-h relationship on loading and unloading, respectively, and γ_p is the constant to be unity for the perfect plasticity.

2.4. Raman Spectroscopy

Highly concentrated stress field seems to be realized under an indentation. In the case of TZP, stress-induced transformation from tetragonal into monoclinic phase can be predicted to occur under the indentation. Raman spectroscopy by using a focused ultraviolet laser with a diameter of 1μm was carried out at the bottom of an indentation to confirm the phase transformation.

3. RESULTS AND DISCUSSION

3.1. Meyer Hardness of Zirconia Polycrystals

The hardness of materials is conventionally evaluated as H_M. The H_M-value is, however, not a measure of the plasticity of ceramics,[7] because it is definitely affected by the elasticity, e.g. Young's Modulus. Therefore, not only grain size dependence but also indentation size dependence of the H_M-value of MZP, TZP and CZP was obscure as reported in previous studies.[5,6] In this study, the evaluation of H_T, a measure of plasticity, for each zirconia was carried out, and then revealed the following indentation size dependence.

3.2. True Hardness of CZP

The H_T-value of CZP increased with a decrease in h_p as shown in Fig.3. Also, the grain size dependence of H_T was hardly observed in CZP. Moreover, the H_T-value of a cubic zirconia single crystal as a function of h_p was superimposed just on that of CZP (see Fig.3). According to the theory of the strain gradient plasticity,[3,4] in which the building-up of geometrically necessary dislocations under an indentation was modeled, the indentation size dependence of hardness is represented as follows,

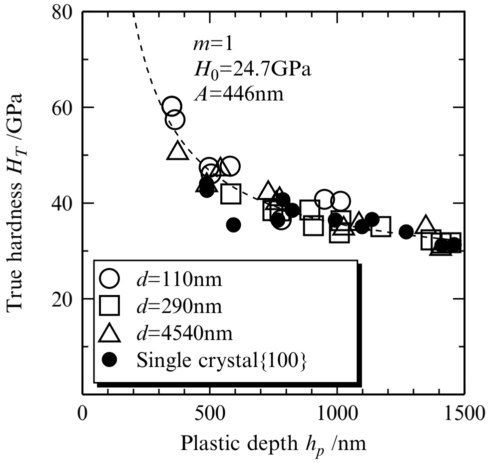

Figure 3. The H_T-value of CZP as a function of h_p. d is the average grain size of CZP. The broken line is drawn by using Eq.(5) with $m = 1$.

$$\left(\frac{H_T}{H_0}\right)^m = 1 + \frac{A}{h_p} \tag{5}$$

where H_0 is the hardness evaluated at $h_p \to \infty$, A is the constant associated with the material characteristic length such as the Burgers vector of the dislocation, and m is the constant to be 1 or 2. The h_p dependence of H_T shown in Fig.3 was well described by using Eq.(5) with $m = 1$. Good agreement between the experimental and theoretical h_p dependence of H_T regardless of grain size indicates that the plastic deformation of CZP at room temperature is simply due to the accumulation of dislocation glide in each grain. The dislocations seem to be piled-up at grain boundary but are not able to go through the boundary into the neighboring grains such as those in metals because of the lack of the number of active slip system. In other words, the contribution of grain boundary sliding to the plasticity of CZP seems to be negligibly small.

3.3. True Hardness of MZP

The H_T-value of MZP, which was much smaller than that of CZP, scarcely depended on h_p as shown in Fig.4. In addition, the H_T-value of MZP remarkably increased with a decrease in the grain size below 100 nm (see Fig.4). The softness of MZP at room temperature is attributed to the plastic deformation caused by the twinning of the monoclinic crystallographic structure.[11] Twinning is quite different from dislocation glide observed in CZP, which is obviously associated with the strain gradient plasticity. That is the reason why h_p dependence of the H_T-value of MZP was hardly observed. In terms of metals, the resistance to plastic deformation due to twinning increases with a decrease in grain size such as the Hall-Petch hardening.[12] Correlation between the twinning and grain size has not been cleared in ceramics. However, the resistance to the twinning of monoclinic zirconia may increase with a decrease in grain size comparably with the size of the twin, which is of the order of 10 nm.[11]

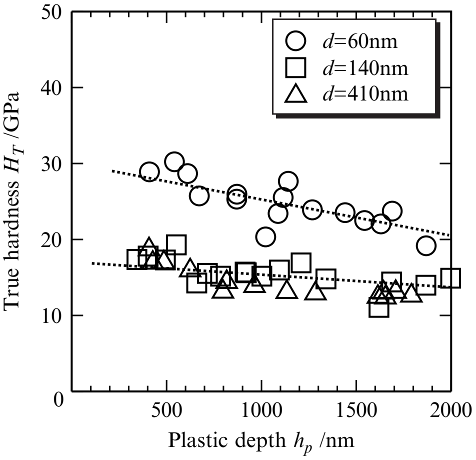

Figure 4. The H_T-value of MZP as a function of h_p. d is the average grain size of MZP.

3.4. True Hardness of TZP

The H_T-value and its h_p dependence of TZP were classified into two categories as a function of grain size. If the grains were larger than 100nm, the H_T-value of TZP was the same as that of MZP and scarcely depended on h_p (see Fig.5). On the contrary, the H_T-value of TZP increased as large as that of CZP and significantly increased with a decrease in h_p if the grain size decreased below 100nm (see Fig.5). As a result of Raman spectroscopy at the bottom of an indentation, the monoclinic phase was observed in the former though only tetragonal phase was detected in the latter. This indicates that the stress-induced transformation from tetragonal to monoclinic phase occurred on loading in the former while it was inhibited in the latter. Therefore, the H_T-value of TZP consisted of grains with a diameter larger than the critical size of the transformation coincided with that of MZP because of the plastic deformation of the transformed monoclinic phase as mentioned above. The decrease of grain size below the critical realizes the stabilization of tetragonal phase.[13] That is the reason why the H_T-value and its h_p dependence of TZP consisted of grains with a diameter less than 100 nm was the same as those of CZP.

4. CONCLUSION

The H_T-value of zirconia polycrystals increased with a decrease in h_p. This is attributed to the building-up of geometrically necessary dislocations under an indentation. In addition, the grain size dependence of H_T was hardly observed. These results indicate that the plastic deformation of zirconia polycrystals at room temperature is basically due to the accumulation of dislocation glide in each grain. In other words, the contribution of grain boundary sliding to the plasticity was negligibly small even if the grains were of the order of 100nm. The H_T-value of MZP, which was much smaller than that of CZP, scarcely depended on h_p because of the plastic deformation due to twinning. The H_T-value and its h_p dependence of TZP

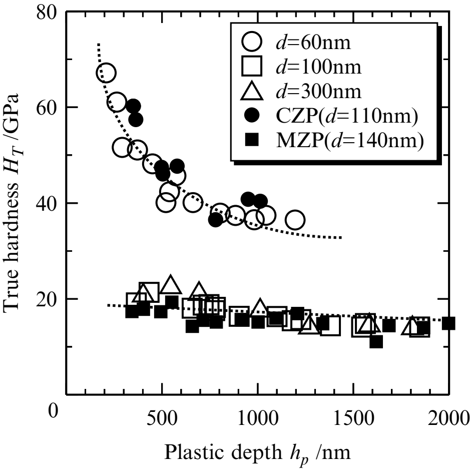

Figure 5. The H_T-value of TZP as a function of h_p. d is the average grain size of zirconia polycrystals.

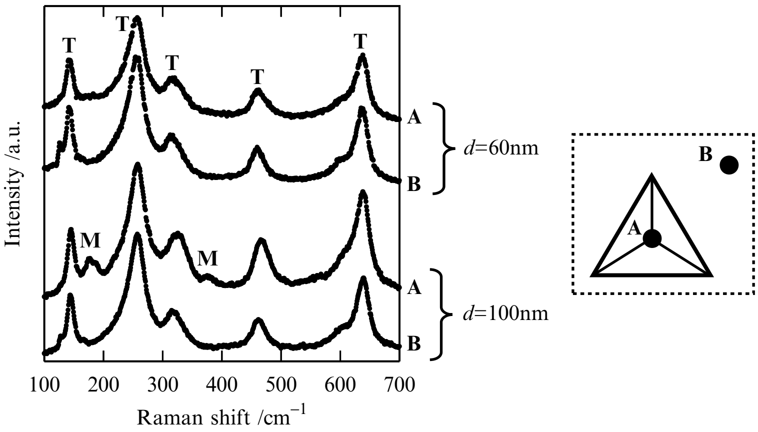

Figure 6. The spectrum of Raman spectroscopy measured at the bottom A of an indentation on TZP. B is the place far from an indentation to obtain the reference spectrum. M and T are assigned to monoclinic and tetragonal phases, respectively. d is the average grain size of TZP.

changed depending on whether the stress-induced phase transformation occurred or not under an indentation, which was determined as a function of grain size.

ACKNOWLEDGEMENT

A part of this research work was supported by the Nippon Sheet Glass Foundation for Materials Science and Engineering and the Grant-in-Aids for Scientific Research (#13750622) of the Ministry of Education, Culture, Sports, Science and Technology, Japan. The authors are grateful to Mr.Y.Teranishi for helping us to carry out Raman spectroscopy.

REFERENCES

1. S.Takeuchi, The Mechanism of the Inverse Hall-Petch Relation of Nanocrystals, *Scripta Mater.* **44**, 1483–1487 (2001).
2. C.A.Schuh, T.G.Nieh, T.Yamasaki, Hall-Petch Breakdown Manifested in abrasive wear resistance of Nanocrystalline nickel, *Scripta Mater.* **46**, 735–740 (2002).
3. W.D.Nix and H.Gao, Indentation Size Effects in Crystalline Materials: A Law for Strain Gradient Plasticity, *J.Mech.Phys.Solids* **46**[3], 411–425 (1998).
4. M.R.Begley and J.W.Hutchinson, The Mechanics of Size-Dependent Indentation, *J.Mech.Phys. Solids* **46**[10], 2049–2068 (1998).
5. R.W.Rice, C.C.Wu, and F.Borchelt, Hardness-Grain-Size Relations in Ceramics, *J.Am.Ceram.Soc.* **77**[10], 2539–2553 (1994).
6. A.Krell, A New Look at the Influences of Load, Grain Size, and Grain Boundaries on the Room Temperature Hardness of Ceramics, *Int'l.J.Ref.Met.Hard Mater.* **16**, 331–335 (1998).
7. M.Sakai, The Meyer Hardness: A Measure for Plasticity?, *J.Mater.Res.* **14**[9], 3630–3639 (1999).
8. M.Yoshida, Y.Shinoda, T.Akatsu, and F.Wakai, Deformation of Monoclinic ZrO_2 Polycrystals and Y_2O_3-Stabilized Tetragonal ZrO_2 Polycrystals Below the Monoclinic-Tetragonal Transition Temperature, *J.Am.Ceram.Soc.* **85**[11], 2834–2836 (2002).
9. M.Sakai, S.Shimizu, and T.Ishikawa, The Indentation Load-Depth Curve of Ceramics, *J.Mater.Res.* **14**[4], 1471–1484 (1999).
10. W.C.Oliver and G.M.Pharr, An Improved Technique for Determining Hardness and Elastic Modulus Using Load and Displacement Sensing Indentation Experiments, *J.Mater.Res.* **7**[6], 1564–1583 (1992).
11. I-W.Chen, Implication of Transformation Plasticity in ZrO_2-Containing Ceramics: II, Elastic-Plastic Indentation, *J.Am.Ceram.Soc.* **69**[3], 189–194 (1986).
12. D.Hull, Effect of Grain Size and Temperature on Slip, Twinning and Fracture in 3% Silicon Iron, *Acta Metall.* **9**[3], 191–204 (1961).
13. F.F.Lange, Transformation Toughening Part 1 Size Effects Associated with the Thermodynamics of Constrained Transformations, *J.Mater.Sci.* **17**, 225–234 (1982).

INDENTATION FRACTURE, ACOUSTIC EMISSION AND MODELLING OF THE MECHANICAL PROPERTIES OF THIN CERAMIC COATINGS

S.J. Bull, I. Arce-Garcia, E.G.-Berasetegui and T.F. Page[†]

ABSTRACT

Fracture is an almost inevitable consequence of highly loaded contacts in ceramic-coated systems. For relatively thick coatings fracture is often similar to that observed in bulk samples of the coating but as the coating thickness is reduced the substrate plays an increasing role in influencing or even controlling fracture behaviour. Both through-thickness and interfacial fracture may be observed depending on the relative toughness of the substrate, coating and interface. Through-thickness fracture is exacerbated by plastic deformation in the substrate and therefore the load support from the substrate is critically important in determining the type and extent of fracture observed. In this paper, nanoindentation testing and post facto atomic force and scanning electron microscopy is used to characterise the types of fracture which occur for hard coatings on softer substrates and multilayer coatings on glass. The effect of fracture on the nanoindentation load-displacement curves and the hardness and Young's Modulus values obtained from them is discussed and a simple model to account for the observed behaviour is introduced. The use of acoustic

---

[†] School of Chemical Engineering and Advanced Materials, University of Newcastle, Newcastle upon Tyne, NE1 7RU, UK

emission to monitor plasticity and fracture during the indentation cycle is also discussed.

1. INTRODUCTION

The durability and performance of coatings in almost every application depend on their as-deposited mechanical properties such as adhesion, hardness, toughness and elastic modulus. These properties may not be the same as those of the same material in bulk form due to different microstructural and defect states arising from the deposition process. As the coating thickness is reduced it becomes increasingly difficult to measure these properties by conventional methods and low load nanoindentation and scratch testing have been developed to enable measurements to be achieved at scales commensurate with the coating thickness. Continuously recording indentation test methods are well established for the determination of Elastic Modulus and hardness.[1,2,3] but methods for assessment of fracture toughness and adhesion are much less developed.[4,5] In part the reason for this is that mechanism of fracture failure around an indentation is complex and depends on the relative properties of coating, substrate and interface and therefore a universal analysis method is unlikely to be produced. However, in some cases it is possible to identify failure modes that are amenable to analysis resulting in reasonable toughness data. Microscopy and analysis of fracture paths is a key part of this approach, particularly as the indentations get smaller.

There are a number of different indentation fracture events which might occur in a coating substrate system (Table 1), the occurrence of which will depend on the relative toughness of coating/substrate and any interfaces present. These failure modes will be altered by plastic deformation in the substrate which can lead to the superposition of bending stresses on to those generated by the indentation.

This paper discusses the type of fracture events which occur for hard coatings on soft and hard substrates and outlines the effect that fracture events have on other mechanical properties measured by indentation (such as hardness and Young's Modulus). It also introduces the use of acoustic emission generation to monitor fracture events in very thin coatings where it is difficult to identify them by conventional microscopy (both scanning electron and atomic force).

2. EXPERIMENTAL

2.1. Sample Preparation

In this study thin ceramic coatings have been deposited onto both brittle and ductile substrates to assess the fracture behaviour of the coating/substrate system. Niobium

Table 1. Fracture events associated with brittle (ceramic) coating/substrate systems.

Substrate	Coating	Fracture type
Ductile	Brittle	Through-thickness fracture, brittle fracture in coating parallel to interface, ductile interfacial fracture, microfracture in coating
Brittle	Brittle	Bulk chipping, through-thickness fracture, brittle interfacial fracture, microfracture in coating, microfracture in substrate